Aalborg Universitet

Bandwidth oriented proportional-integral controller design for back-to-back power converters in DFIG wind turbine system

Zhou, Dao; Blaabjerg, Frede

Link to publication from Aalborg University

Bandwidth Oriented PI Controller Design for Back-to-Back Power Converters in DFIG Wind Turbine System

Dao Zhou[*], Frede Blaabjerg

Department of Energy Technology, Aalborg University, Aalborg, DK-9220, Denmark
[*] *Email: zda@et.aau.dk*

Abstract: The Doubly-Fed Induction Generator (DFIG) system currently occupies close to 50% of the wind energy market. The vector control is the proven and state-of-the-art solution for its back-to-back power converters by using the dual-loop controller design: the inner current and the outer voltage/power. This paper focuses on the modelling of power converters and the parameters design of PI controller. According to the Bode plots, the relationship among the switching frequency, inner loop bandwidth, and outer loop bandwidth can be found. At least one tenth difference between them is necessary for the sake of either the switching harmonic mitigation or the fully decouple of the dual loops. The procedure to design bandwidth for the grid-side converter and the rotor-side converter are thoroughly addressed and explained on a real-scale 2 MW and a down-scaled 7.5 kW DFIG systems. On the basis of the relationship between the controller bandwidth and the rise time, the theoretically designed bandwidth is able to be verified in both the simulation and the experiment.

1. Introduction

In recent years, the electricity production from the wind, solar, hydro, geothermal, tidal and biomass energy sources has arrived and been developed with increasing attention. Particularly, the wind energy has become mainstream and competitive with conventional resources [1]. According to the popular models of top 10 wind turbine manufacturer in 2013, the constant speed system is continuously being faded out by the stricter grid connection requirements, whereas the variable speed system becomes overwhelming [2]. Although the wind turbine system can be categorized into several concepts in terms of the generator type, with and without the gearbox, or the rating of the power electronic converter, it is common to divide the wind turbine system into a partial-scale power converter equipped with a Doubly-Fed Induction Generator (DFIG) and a full-scale power converter together with either a Synchronous Generator (SG) or an Induction Generator (IG) [1], [3]. Currently, the configuration of the DFIG system occupies close to 50% of the wind energy market, due to its light weight, small size, and cost-effectiveness of the generator, as well as the relatively small and economical power converter [4], [5].

As shown in 0, the stator circuit of the DFIG is directly linked to the power grid, while the rotor side is connected to the grid through the back-to-back power converters. They are named as the Rotor-Side Converter (RSC) and the Grid-Side Converter (GSC) due to their positions. In respect to the control scheme of the RSC, the vector control and the direct control are the most commonly used and representative techniques [6]-[11]. The vector control can be further divided into the stator Flux Oriented Control (FOC) and the stator Voltage Oriented Control (VOC) by the different orientations of the

synchronous rotating frame. If the flux vector is aligned to the d-axis of the rotating frame, the decoupled control of the electromagnetic torque and the excitation current in the FOC are able to be achieved. In the case that the voltage vector is aligned, the independent active power and reactive power can be realized using the VOC [8], [9]. Meanwhile, the direct control can be further classified as the Direct Torque Control (DTC) and the Direct Power Control (DPC) with the control objectives of electromagnetic torque together with rotor flux, and the active power together with the reactive power, respectively [10], [11]. Compared with the vector control, although the direct control may have advantages of the easy-implementing algorithm, fast response and better robust, the switching frequency is not fixed, which results in fluctuations of the electromagnetic torque, generator current and flux, and might cause the reduced reliability of the gearbox. As a consequence, the vector control is more widely adopted in industry applications.

Under the synchronous reference frame, the component of the current reference becomes a dc-quantity. Hence, a zero steady-state error can be obtained by employing a standard integrator due to its infinite gain at zero frequency. A lot of research efforts are recently devoted to the Proportional-Resonant (PR) controller under the stationary reference frame, because the infinite gain can similarly be achieved at the desired ac frequency by using the resonant controller [12]-[14]. However, although the stationary reference frame is independent on the phase angle, a Phase-Locked Loop (PLL) is still prerequisite at the generation of the current reference. If the harmonics compensation is not taken into account, the Proportional-Integral (PI) controller under the synchronous reference frame is exactly equivalent with the PR controller under the stationary reference frame [14].
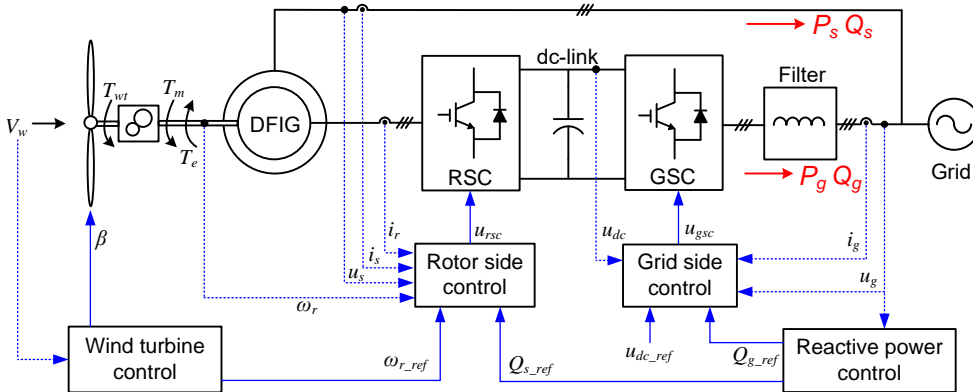
Typical control strategies of back-to-back power converters in a doubly-fed induction generator wind turbine system (GSC: Grid-Side Converter, RSC: Rotor-Side Converter)

A step-by-step design procedure of PI controllers for inner current and outer dc-link voltage is addressed according to the mathematical modelling of the GSC and the optimum design from the control theory [15], [16]. However, the frequency domain oriented designed controller cannot easily be verified in the time domain based experimental setup. With the help of the Bode plots, this paper introduces a

standard design procedure of the PI controller on the basis of the desired bandwidth. Moreover, the relationship between the bandwidth in the frequency domain and the step response in the time domain can be found, which proves the designed bandwidth by using a step change. Meanwhile, the dual loop design of the controllers can be extended to the RSC as well.

The remaining parts of this paper are organized as follows. It starts with the modelling and the controller design of the GSC and the RSC. Afterwards, the designed bandwidth is verified by the simulation and experiment in terms of the step response. Finally, some conclusions are drawn in the last section.

1. Modelling and controller design of grid-side converter

In respect to a three-phase PWM power converter, the cascaded control structure is normally employed, including the inner-current loop and the outer-voltage/power/speed/flux loop. Aiming at the grid-tied application, in order to keep a fixed dc-link voltage and a unity power factor, the control structure of the GSC is shown in Fig. 1. Although the *LCL* filter is widely adopted, as a single inductor filter has the similar characteristic compared to the *LCL* filter within low frequency [17], this type is applied in this paper. Specifically, the two grid current controllers are employed to realize the fast response during the varying loading conditions, and a dc-link voltage controller is applied to maintain a constant dc voltage enabling the decouple control of the back-to-back power converters.
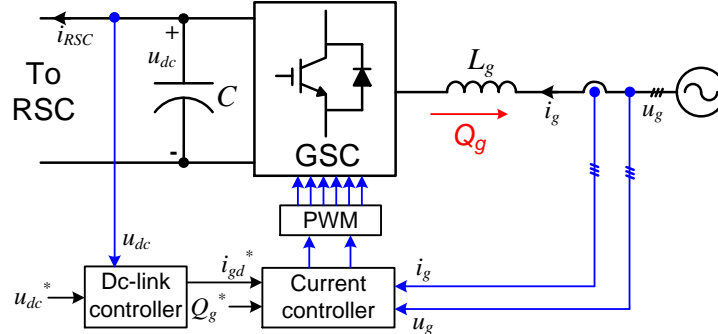
Fig. 1 *Control structure of grid-side converter using inductor filter*

1.1. Modelling of grid-side converter

Due to the utilization of the power electronic semiconductor, featuring as a switching device, the control system inevitably becomes discontinuous. Inspired by the dynamic modelling of the dc/dc converter, a state-average approach can be used to enable the circuit model continuous. However, different from the dc/dc converter, a time-varying ac voltage in the input side induces that the quiescent operation point can hardly be found without the introduction of the synchronous reference frame (*dq* frame), which transfers the static three-phase system to the rotating two-phase system.

As mentioned in [18], a PLL based on the inverse Park transformation is applied to realize grid synchronization, but its effect on the modelling of the power converter is out of the scope of this paper. In the case of the *dq* transformation, together with the negligence about the parasitic resistance of the inductor, the state equations of the boost inductor current and dc-link capacitor can be obtained [16],

$$
\begin{cases}
\dfrac{d}{dt}\begin{bmatrix} i_{gd} \\ i_{gq} \end{bmatrix} = \dfrac{1}{L_g}\begin{bmatrix} u_{gd} \\ u_{gq} \end{bmatrix} - \begin{bmatrix} 0 & -\omega_1 \\ \omega_1 & 0 \end{bmatrix}\begin{bmatrix} i_{gd} \\ i_{gq} \end{bmatrix} - \dfrac{1}{L_g}\begin{bmatrix} d_d \\ d_q \end{bmatrix}u_{dc} \\[4mm]
\dfrac{d}{dt}u_{dc} = \dfrac{3}{2C}\begin{bmatrix} d_d \\ d_q \end{bmatrix}^T\begin{bmatrix} i_{gd} \\ i_{gq} \end{bmatrix} - \dfrac{1}{C}i_{RSC}
\end{cases}
\tag{1}
$$

where u_g denotes the grid voltage; i_g denotes the ac-side current; ω_1 denotes the grid angular frequency; d denotes the duty cycle; and subscripts *dq* denote the variables under *dq* frame. u_{dc} is the dc voltage; i_{RSC} is the loading current from the RSC; and L_g and C are the boost inductance and the dc capacitance, respectively. It is noted that the coupling components in the first equation is introduced by the Park transformation, and a constant of 3/2 appears in the second equation due to the fact that an equal amplitude transformation results in the different transformed power.

1.2. Controller design of inner-current loop

Associated with (1), the transfer function from the duty cycle to the output voltage of the power converter is simply and merely considered as a proportion unit. In reality, due to the transport delay induced by the PWM modulation and the sampling delay caused by the digital control [19], an equivalent delay unit is more reliable and acceptable. As mentioned in [19], [20], a symmetrical and an asymmetrical PWM can be achieved by a single and double sampling within a switching period, the delay time of these two samplings can be considered as 5/4 and 3/4 of the switching period, respectively. Moreover, as the delay time is around hundreds of the micro-second due to the high switching frequency, the delay unit can roughly be regarded as an inertia unit $G_{PWM}(s)$ [20],

$$
G_{PWM}(s) = \frac{1}{T_d s + 1}
\tag{2}
$$

where T_d is the inertia of the PWM converter, and it becomes different when the symmetrical and asymmetrical PWM are applied.

During the tuning of the inner current loop, the dc voltage can be considered constant due to its much slower response. By using the grid VOC together with the first equation of (1), a linear control plant can be obtained by the introduction of the perturbation [21]. The control block diagram of the grid current is depicted in Fig. 2a together with the aforementioned PMW model. In order to avoid the influence of the

coupling components, the current feedforward is adopted. Simultaneously, a PI controller $G_{PI\_ig}(s)$ is adopted to realize the error-free tracking with the transfer function,

$$G_{PI\_ig}(s) = K_{p\_ig} + \frac{K_{i\_ig}}{s} \qquad (3)$$

where K_{p_ig} and K_{i_ig} represent the proportional and the integral coefficients of the PI controller.

a

b

c
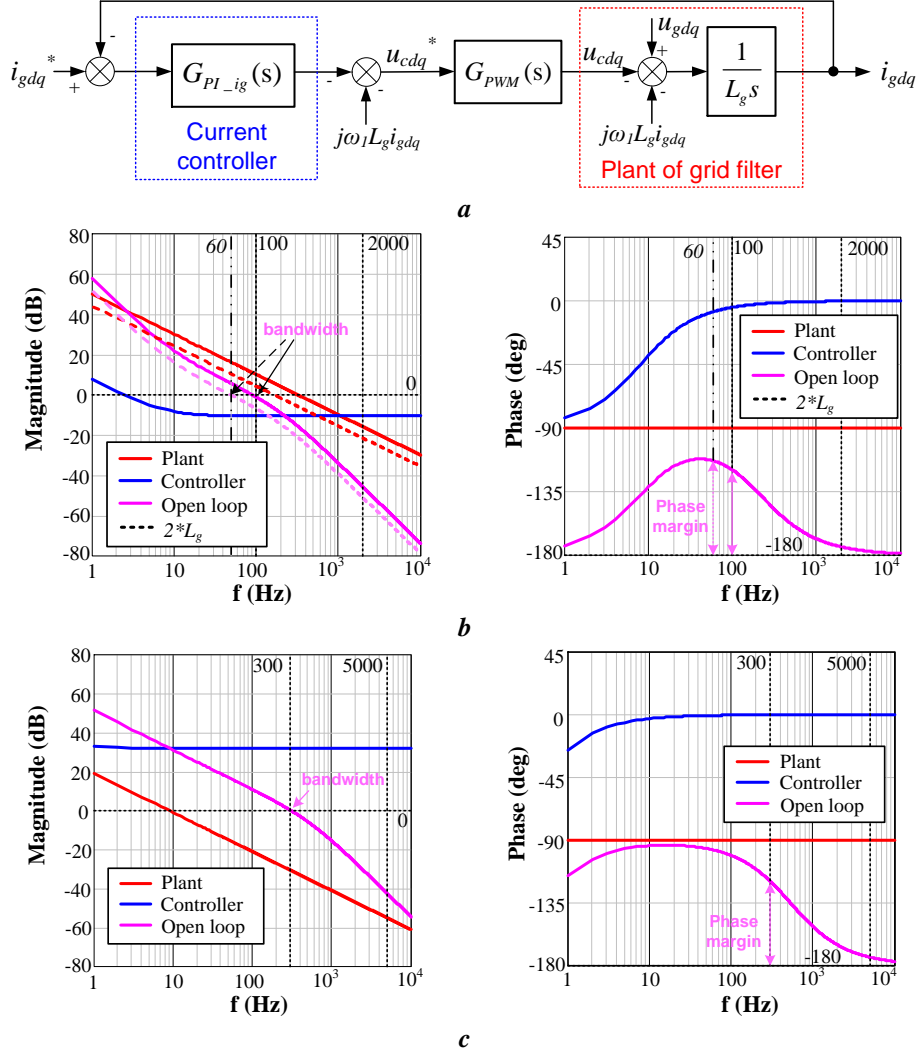
Fig. 2 *Grid current loop control in the grid-side converter*

a Block diagram
b Bode plots of open-loop current transfer function in 2 MW system
c Bode plots of open-loop current transfer function in 7.5 kW system

Although the PI controller can be design by the optimum control theory design, the zero-pole displacement, or the root-locus analysis [15], [21], [22], the Bode plots is applied with the design criterion of the crossover frequency and its corresponding phase margin. To achieve a fast response during the perturbation, the design target of the PI controller is to regulate the bandwidth of the current loop between 1/20 and 1/10 of the switching frequency. Meanwhile, the amplitude curve of the open-loop transfer

function rides through 0 dB with the slope rate -20 dB/dec in order to avoid the stability issue and guarantee a sufficient phase margin (normally higher than 45º).

The parameters of the GSC in a real-scale 2 MW and a down-scaled 7.5 kW DFIG systems are listed in Table 1. It is worth noting that the single sample within a switching frequency is applied in the 2 MW system, while the double sample is used in the 7.5 kW system. Together with the proportional and integral coefficients of the current controller, the boost inductance as well as the switching frequency, the transfer function of the control plant, the current controller and the open-loop grid current can be obtained.

Table 1 Parameters of grid current loop in 2 MW and 7.5 kW DFIG systems

	2 MW	7.5 kW
Grid peak phase voltage U_g (V)	563	311
Dc-link voltage V_{dc} (V)	1050	650
Boost inductor L_g (mH)	0.5	18
Sampling freqency f_{sa} (kHz)	2	10
Switching freqency f_{sw} (kHz)	2	5
Delay time in PWM T_d (µs)	625	250
Proportional coefficient of PI controller K_{p_ig}	0.3	40
Integral coefficient of PI controller K_{i_ig}	15	120

In the case of the 2 MW system, the Bode plots are shown in Fig. 2b. It can be seen that the control plant of the grid filter keeps the slope -20 dB/dec because of its intrinsic zero-point pole. With the help of the current controller, which contains a zero-point pole and a desired zero, the bandwidth of the grid current is able to be set at 100 Hz, 1/20 of the switching frequency. Simultaneously, the turning frequency of the PI controller is set at 8 Hz, which results in a phase margin of 60.2º, enabling a stable design of the grid current loop. Moreover, due to the introduction of the pole around 1/10 switching frequency of the PWM delay unit, another -20 dB/dec is superposed in the open-loop grid current transfer function, which prevents the high bandwidth design due to the decrease of the phase margin. To verify the robustness of the controller design, the Bode plots of the grid-current open loop is compared with the case that the filter inductance becomes two times of the original value. As shown in Fig. 2b, due to the higher inertia of the modified inductor, the bandwidth of the current loop becomes 60 Hz with the originally designed PI parameters, and the phase margin increases remarkably. It is indicated that the grid current loop is still stable but with lower response time.

Similarly, the Bode plots of 7.5 kW system is depicted in Fig. 2c. It can be seen that, the turning frequency introduced by the PWM delay unit is relatively higher than the 2 MW system due to the less delay of the asymmetrical PWM modulation, which enables the higher bandwidth design of the grid current. Thus, with a 0.5 Hz turning frequency of the PI controller, the bandwidth of the current loop is regulated at 300 Hz with a phase margin of 60.4º.

1.3. Controller design of outer-voltage loop

Considering the controller design of the outer voltage loop, the inner current loop can be regarded as a closed-loop unit $G_{cl\_ig}(s)$ derived from Fig. 2a. According to the second equation of (1), a linear plant of dc-link capacitor is roughly derived by neglecting the perturbations from the second-order terms, and the duty cycle [21]. Moreover, as the static duty cycle in d-axis is normally much higher than q-axis, the static d-axis duty cycle is solely considered, which equals the line voltage amplitude over the dc-link voltage. Together with the voltage controller $G_{PI\_V}(s)$, the block diagram of the dc voltage control can be obtained as shown in Fig. 3a. It is noted that a filter unit $G_f(s)$ is employed in the feedback loop in order to remove the high-frequency noise during the sampling.

For the sake of the separation between the inner loop and the outer loop, the bandwidth of the outer loop is limited from 1/50 to 1/10 of the inner loop. By this approach, during the design of the inner loop, the control objective of the outer loop can be regarded as a constant due to its much slower response. On the other hand, during the tuning process of the outer loop, the gain of the inner closed loop behaves like a unit proportion unit within the outer loop bandwidth, which simplifies the PI controller design. Alternatively, due to its high enough open-loop gain, the inner loop can fully track the reference within the bandwidth of the outer loop, which causes that the closed inner loop seldom affects the controller design of the outer loop.

Table 2 Parameters of voltage loop in 2 MW and 7.5 kW DFIG systems

	2 MW	7.5 kW
Dc-link capacitor C (μF)	20,000	600
Filter time constant T_f (ms)	0.001	10
Proportional coefficient of PI controller K_{p_V}	2	0.1
Integral coefficient of PI controller K_{i_V}	10	0.5

With the dc-link capacitance, the time constant of the first-order filter as well as the proportional and integral coefficients of the voltage PI controller listed in Table 2, the transfer function of the control plant, the voltage controller and the open-loop dc voltage can be obtained. In the 2 MW system, the Bode plots are shown in Fig. 3b. It can be seen that, the control plant keeps -20 dB/dec due to its zero-point pole. Moreover, the amplitude characteristic of the closed-loop grid current maintains 0 dB within the crossover frequency, while its slope becomes -40 dB/dec beyond the crossover frequency. Moreover, with a time constant of several micro-seconds introduced by the first-order filter, the amplitude curve hardly changes within the switching frequency. Finally, with the proper design of the PI controller, the bandwidth of the dc voltage loop is set at 5 Hz, 1/20 of the inner loop bandwidth, with a phase margin of 80.2º.
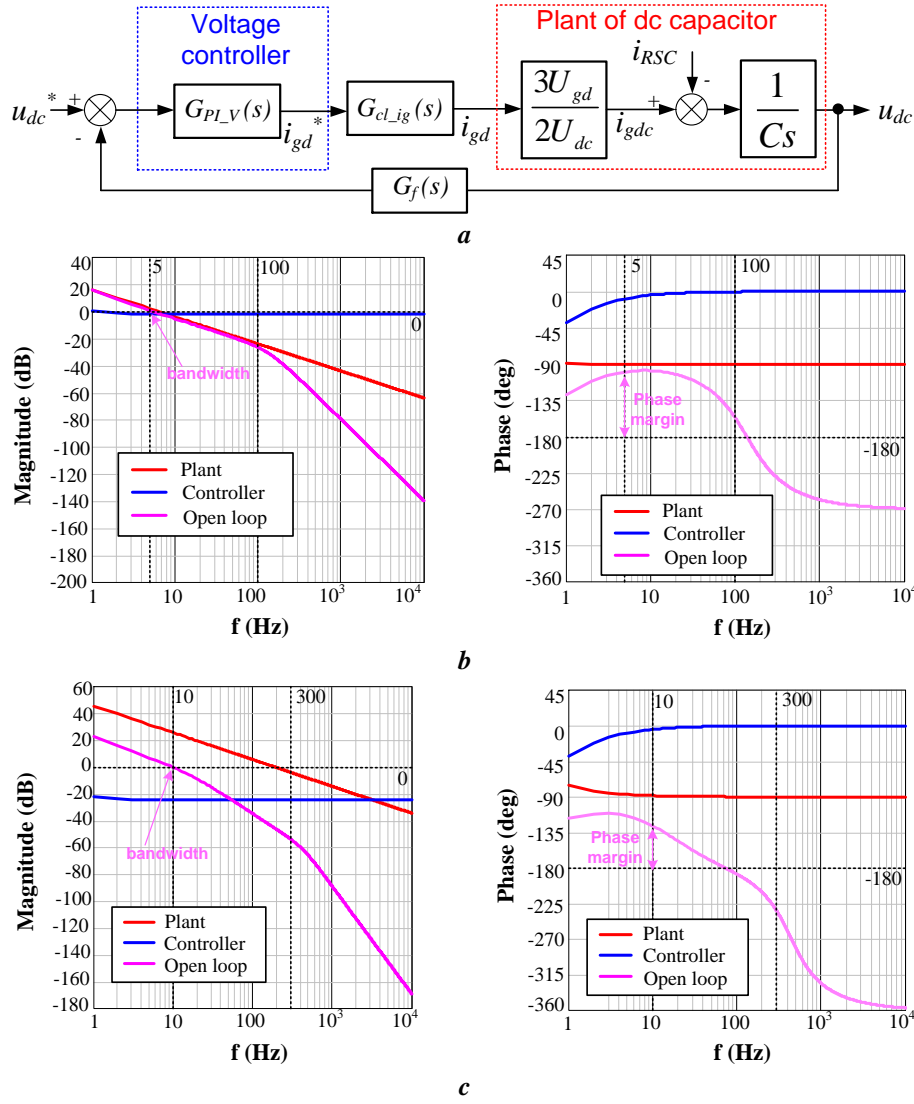
Fig. 3 *Dc voltage loop control in the grid-side converter*

a Block diagram
b Bode plots of open-loop voltage transfer function in 2 MW system
c Bode plots of open-loop voltage transfer function in 7.5 kW system

Similarly, the Bode plots of the 7.5 kW system are shown in Fig. 3c. When the frequency is higher than the crossover frequency of the sampling filter, an additional slope -20 dB/dec is superposed. The amplitude curve eventually behaves with a slope -80 dB/dec when the frequency is higher than the grid current bandwidth. However, the PI controller is able to adjust the bandwidth of the voltage loop at 10 Hz with a phase margin of 53.2°.

## 2. Modelling and controller design of rotor-side converter

As mentioned before, the GSC simply contains an inductor between the voltage source converter and the power grid. However, the RSC employs a DFIG in between, where the rotor of the DFIG is connected

to the converter, and the stator of the DFIG is linked to the power grid. Dynamically, as the DFIG is much more complicated compared to the inductor, this section starts with its modelling.

2.1. Modelling of rotor-side converter

With the transformation under the synchronous rotating frame and rotor variables referred to the stator-side, the mathematical model of the DFIG can be simplified with reduced order and shown in Fig. 4a in terms of the voltage equation and the flux equation [6]. With the stator voltage aligned to the d-axis of the synchronous reference frame, neglecting the stator resistance, usually very low for the large induction generator, the relationship between the rotor voltage and the rotor current can be found,

$$\frac{d}{dt}\begin{bmatrix} i_{rd}^{'} \\ i_{rq}^{'} \end{bmatrix} = \frac{1}{\sigma L_r}\begin{bmatrix} u_{rd}^{'} \\ u_{rq}^{'} \end{bmatrix} + \begin{bmatrix} -\dfrac{R_r}{\sigma L_r} & \omega_s \\ -\omega_s & -\dfrac{R_r}{\sigma L_r} \end{bmatrix}\begin{bmatrix} i_{rd}^{'} \\ i_{rq}^{'} \end{bmatrix} - \begin{bmatrix} \dfrac{s_l L_m}{\sigma L_r L_s} \\ 0 \end{bmatrix} u_{sd} \tag{4}$$
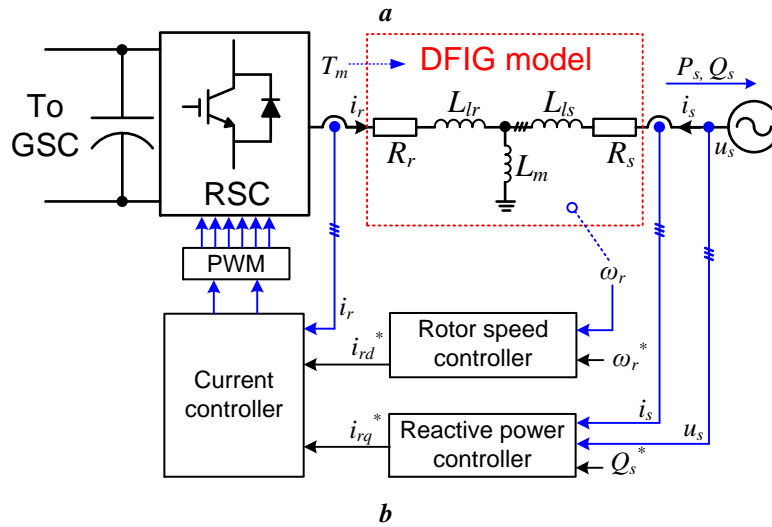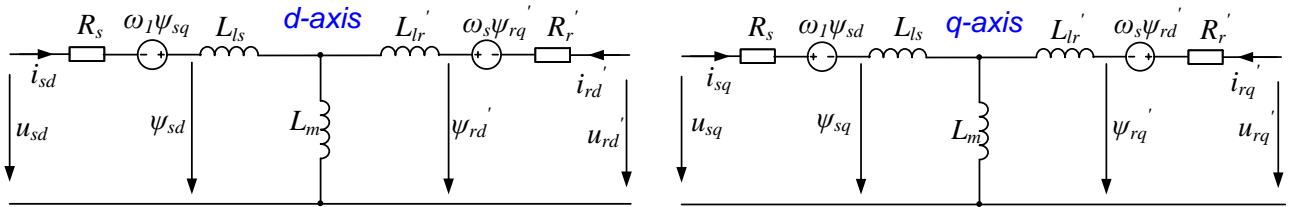
Fig. 4 *Modelling of DFIG and its control under synchronous rotating frame*
a Equivalent circuit of DFIG under d-axis and q-axis
b Control structure of rotor-side converter

where u_s, u_r denote the stator and rotor voltage, i_s, i_r denote the stator and rotor current, ψ_s, ψ_r denote the stator and rotor flux, R_s, R_r denotes the stator and rotor resistance, and L_s, L_r and L_m denote the stator inductance, rotor inductance and magnetizing inductance, respectively. σ represents the leakage coefficient,

9

and equals to $(L_s L_r - L_m^2)/L_s L_r$, ω_s represents the slip angular frequency, and sl denotes the slip of the induction generator, and equals to ω_s/ω_1. The superscript ´ means rotor variables referred to the stator side.

Also, the stator-side active power P_s and reactive power Q_s can be expressed by,

$$\begin{cases} P_s = \dfrac{3}{2} u_{sd} i_{sd} = -\dfrac{3}{2} \dfrac{L_m u_{sd}}{L_s} i'_{rd} \\ Q_s = -\dfrac{3}{2} u_{sd} i_{sq} = \dfrac{3}{2} (\dfrac{u_{sd}^2}{\omega_1 L_s} + \dfrac{L_m u_{sd}}{L_s} i'_{rq}) \end{cases} \tag{5}$$

Since the DFIG electromagnetic torque T_e is the stator active power over the grid angular frequency, the DFIG rotor speed ω_r can be jointly determined by the d-axis rotor current and the shaft torque T_m introduced from the turbine rotation,

$$\frac{d}{dt}\omega_r = \frac{1}{J}(T_e - T_m) \tag{6}$$

According to (5), the rotor current in q-axis is not only related to the reactive power, but also coupled to the stator inductance. Due to the reduced magnetizing inductance during the normal operation, the rotor reference in q-axis cannot be determined by the defined reactive power. As a consequence, a closed-loop control of the reactive power is required due to its sensitivity on the parameters of the induction generator. Similar with the GSC, the cascaded control structure is implemented in the RSC as shown in Fig. 4b. The rotor current is controlled as the inner loop, while the stator-side reactive power and rotor speed are regulated as the outer loop.

2.2. Modelling of inner-current loop

The relationship between the rotor voltage and the rotor current is illustrated in (4), which is established with the rotor-side variables referred to the stator-side. In the realistic control system, with the relationship of the rotor voltage and current by using the winding ratio between the stator-side and rotor-side k_{sr}, the control plant referred to the rotor-side can be obtained as shown in Fig. 5a. Considering the same PWM model as the GSC and the PI controller of the rotor current $G_{PI\_ir(s)}$, the control block diagram of the rotor current loop can then be obtained.

The parameters of 2 MW and 7.5 kW DFIGs are listed in Table 3, where the switching frequency is decreased with the higher power rating. According to parameters of DFIG, and the current controller, the Bode plots of the control plant, current controller and open-loop rotor current can be obtained as shown in Fig. 5b and Fig. 5c.
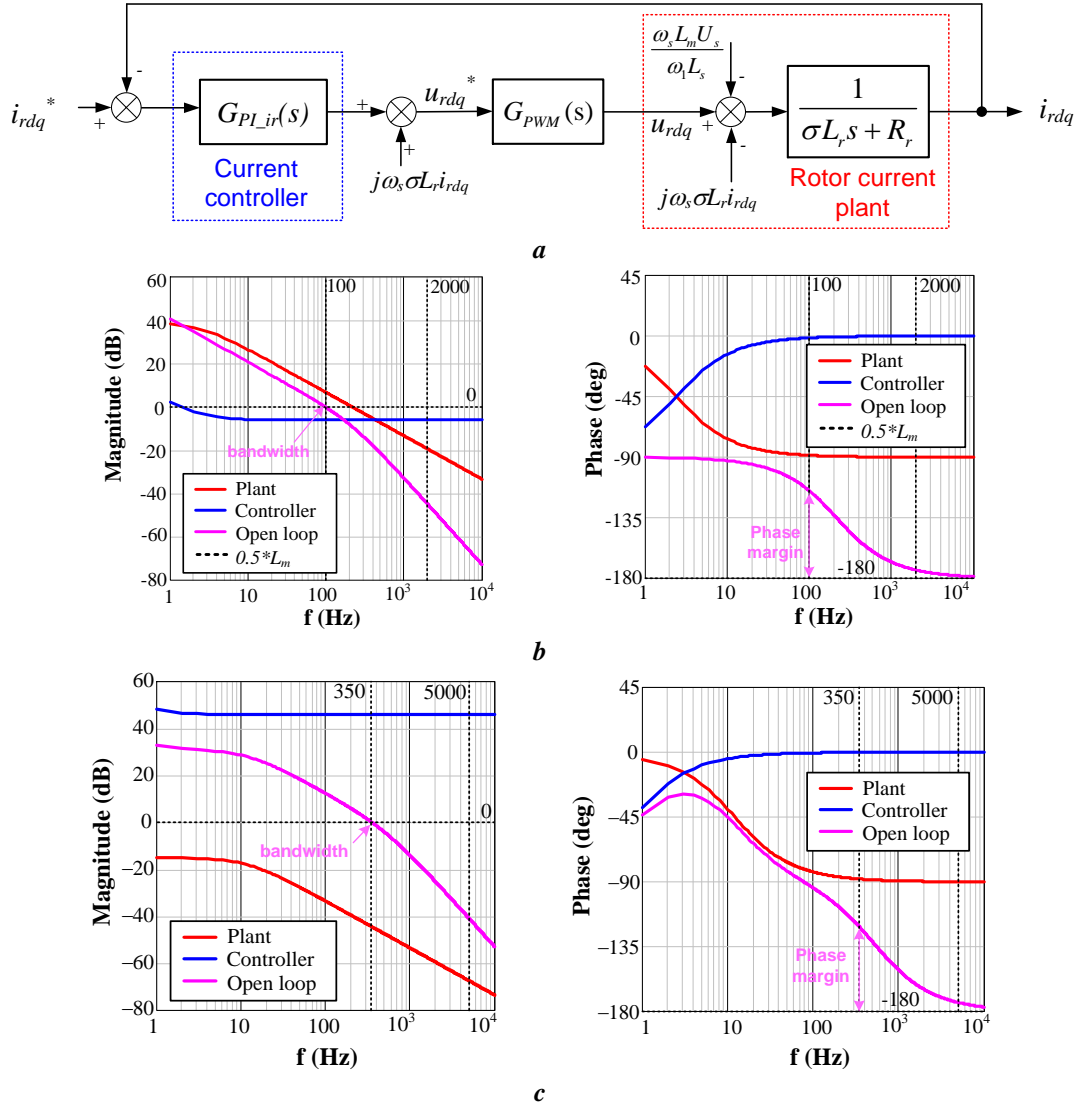
Fig. 5 *Rotor current loop control in the rotor-side converter*

a Block diagram
b Bode plots of open-loop rotor current transfer function in 2 MW system
c Bode plots of open-loop rotor current transfer function in 7.5 kW system

In respect to the 2 MW system, the amplitude curve of the control plant starts with a constant magnitude, but it bends to -20 dB/dec afterwards due to its 2.4 Hz pole. Besides, a 255 Hz pole of the delay unit causes another -20 dB/dec bending in the open-loop. In order to realize the amplitude curve of the open-loop rotor current to crossover 0 dB with the slope -20 dB/dec, its bandwidth is regulated at 100 Hz, 1/20 of the switching frequency. Meanwhile, the zero of the PI controller is designed to counteract the pole of the control plant for the sake of the constant -20 dB/dec before the crossover frequency. Viewed from the stability issues, a phase margin of 64.8° can be achieved. During the DFIG operation, as the magnetizing inductance decreases due to the magnetic saturation, a half value of the magnetizing

11

inductance is assumed. However, the open-loop Bode plots of the rotor current is almost the same with the original magnetizing inductance, because the transfer function of the rotor current plant is determined by the sum of the leakage stator and rotor inductance.

Table 3 Parameters of rotor-side converter and generator in 2 MW and 7.5 kW DFIG systems (referred to stator-side)

	2 MW	7.5 kW
Stator peak phase voltage U_s (V)	563	311
Stator resistance R_s (mΩ)	1.69	440
Stator inductance L_s (mH)	2.95	82.74
Rotor resistance R_r (mΩ)	1.52	640
Rotor inductance L_r (mH)	2.97	84.46
Magnetizing inductance L_m (mH)	2.91	79.30
Leakage coefficient σ	0.03	0.10
Winding ratio between stator and rotor k_{sr}	0.369	0.336
Sampling freqency f_{sa} (kHz)	2	10
Switching freqency f_{sw} (kHz)	2	5
Delay time introduced by PWM T_d (µs)	625	250
Proportional coeffcient of current controller K_{p_ir}	0.5	200
Integral coefficient of current controller K_{i_ir}	7.5	1000

Similarly, the Bode plots of the 7.5 kW system are shown in Fig. 5c. It can be seen that the crossover frequency of the open-loop rotor current is adjusted at 350 Hz, between 1/20 and 1/10 of the switching frequency. Meanwhile, the amplitude curve still crosses over 0 dB with the slope -20 dB/dec, and it ensures a phase margin of 58.4º.

2.3. Controller design of outer-power/speed loop

Together with (5) and (6), the control plant of the reactive power and the rotor speed can be established as shown in Fig. 6a, and the PI controllers $G_{PI\_Q}(s)$ and $G_{PI\_\omega}(s)$ are applied to realize the closed loop. Meanwhile, the control of the rotor current can be considered as the closed loop unit $G_{cl\_ir}(s)$.

Table 4 Parameters of power controller in 2 MW and 7.5 kW DFIG systems (referred to stator-side)

	2 MW	7.5 kW
Proportional coefficient of power controller K_{p_Q}	0.00009	0.0003
Integral coefficient of power controller K_{i_Q}	0.0135	0.45
Proportional coefficient of rotor speed controller K_{p_ω}	1200	
Integral coefficient of rotor speed controller K_{i_ω}	3600	/
Inertia of the induction machine J (kg*m^2)	338	

As aforementioned, to independently design the inner loop and the outer loop, the design principle of the reactive power PI controller is to regulate the bandwidth of outer loop between 1/20 and 1/10 of the
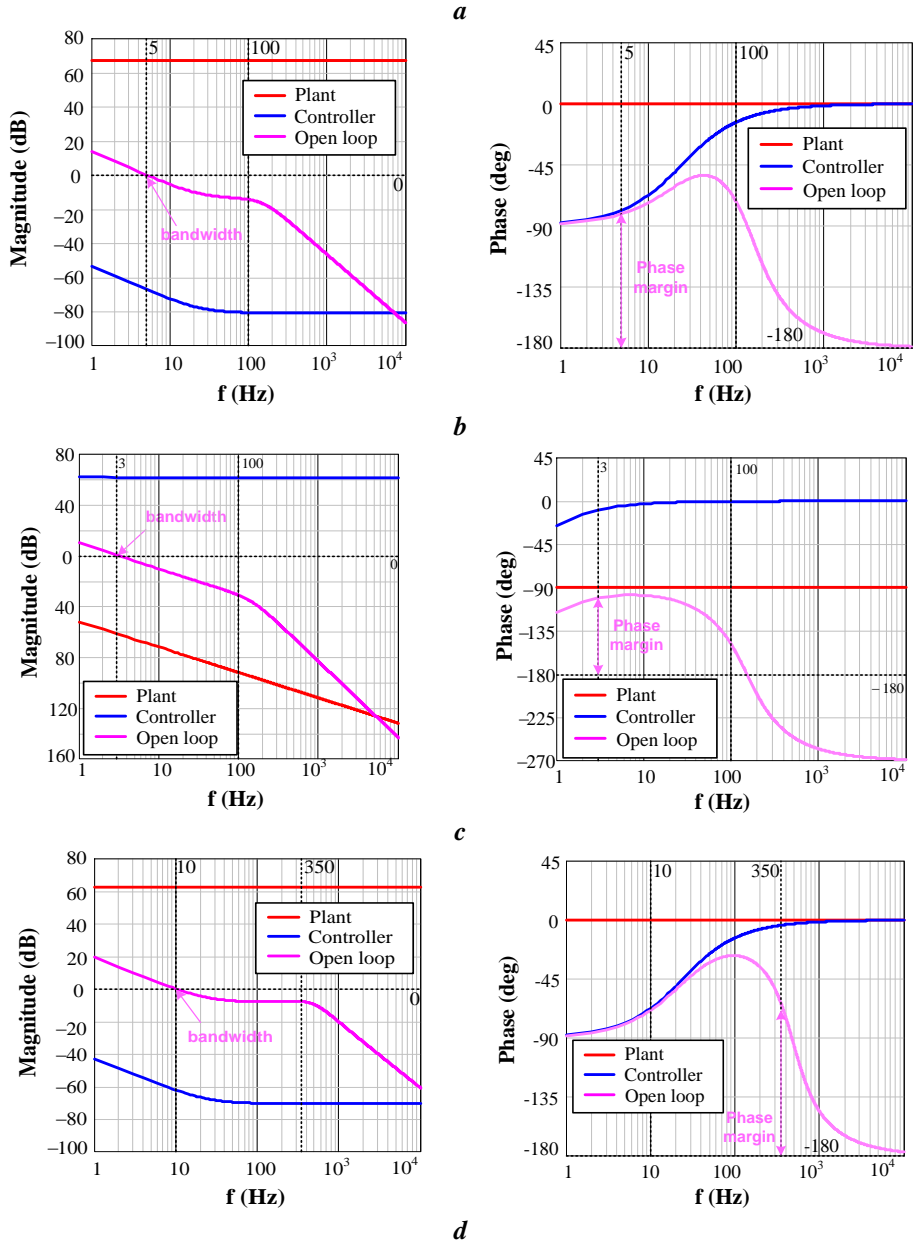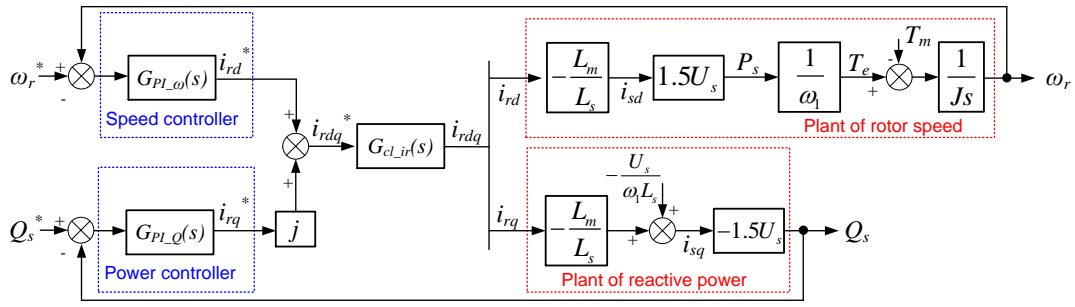
Fig. 6 *Reactive power loop in the rotor-side converter*

a Block diagram
b Bode plots of open-loop reactive power transfer function in 2 MW system
c Bode plots of open-loop rotor speed transfer function in 2 MW system
d Bode plots of open-loop reactive power transfer function in 7.5 kW system

inner loop. At the same time, the amplitude curve is required to cross over the bandwidth with the slope -20 dB/dec seen from the stability point of view.

In respect to the 2 MW DFIG system, with PI parameters of the outer controllers listed in Table 4, the Bode plots of the open-loop reactive power and the rotor speed are depicted in Fig. 6b and Fig. 6c. It is evident that the amplitude and the phase curves of the reactive power plant perform as a proportion unit, and the bandwidth of the reactive power loop is set at 5 Hz with a phase margin of 99.1º. Additionally, if the frequency is higher than inner current loop, it can be seen that the amplitude curve bends with the slope -40 dB/dec, and the phase angle approaches -180º due to two poles introduced by the transfer function of the closed-loop rotor current. Because of the high inertia of the MW-level generator, a low bandwidth of the rotor speed is required (e.g. 3 Hz) to prevent the rotor speed overshoot during the disturbance. For the 7.5 kW system, the bandwidth of the reactive power is set at 10 Hz because of its faster inner current response, and the phase margin can be kept at 111.3º. Furthermore, as the wind turbine is emulated by a prime motor in the experiment setup, the rotor speed loop can be neglected.

3. Simulation and experimental results

The aforementioned bandwidth design is achieved in the frequency domain, which is not easy to be validated by the time-domain simulations and experiments. In order to create the connection between the frequency domain and the time domain, the relationship of concepts used in the frequency domain (like bandwidth, phase margin) and the time domain (e.g. delay time, rise time, peak time, etc.) is a necessity. In the first-order and second-order systems, it is proven that there is strict relationship between the bandwidth and the rise time, where the time interval is defined as between 10% and 90% of steady-state value [20], [23]. Furthermore, even in the high-order system, it can in many cases be equivalent to the first-order or the second-order system by ignoring minor poles but the keeping the dominant poles [23].

In the loop design of the DFIG system, in respect to the inner loop, the control plant of back-to-back power converters can be considered as an inertial unit. The PWM inertia unit can be omitted because of the much higher frequency of the pole compared to the designed bandwidth, and the open-loop transfer function can be considered as an integral unit, because the designed zero point of the PI controller is able to counteract the pole of the control plant. In respect to the outer loop, there is a slight difference between the GSC and the RSC. For the dc voltage outer loop, the control plant is theoretically an integral unit, but it can be regarded as the inertia unit if the equivalent loading resistance is taken into account. As the closed-loop inner current almost performs as a unity transfer function within its bandwidth, together with the PI controller, the open-loop dc voltage can be considered as an integral unit as well. For the reactive

power outer loop, although its control plant is a proportion unit, a PI controller can still make the open-loop transfer function an integral unit by tuning the frequency of the PI controller lower than the bandwidth of the outer loop. As a consequence, the open-loop transfer function of the inner current and outer dc/power is the integral unit, both of which become a first-order system in the case of the closed-loop.

For the first-order system, the relationship between the bandwidth and the rise time during a step can be found [23],

$$f_{BW} \cdot t_r = 0.35 \tag{7}$$

where f_{BW} denotes the bandwidth, and t_r denotes the rise time during the step response. Based on (7), the expected rise time of the inner loop and outer loop can be calculated.

3.1. Simulation validation

A simulation platform of the 2 MW DFIG system is established in Matlab Simulink, whose parameters exactly follow the aforementioned Table 1-4. Accordingly, the step changes can be applied at the various loops in order to verify the bandwidth design.
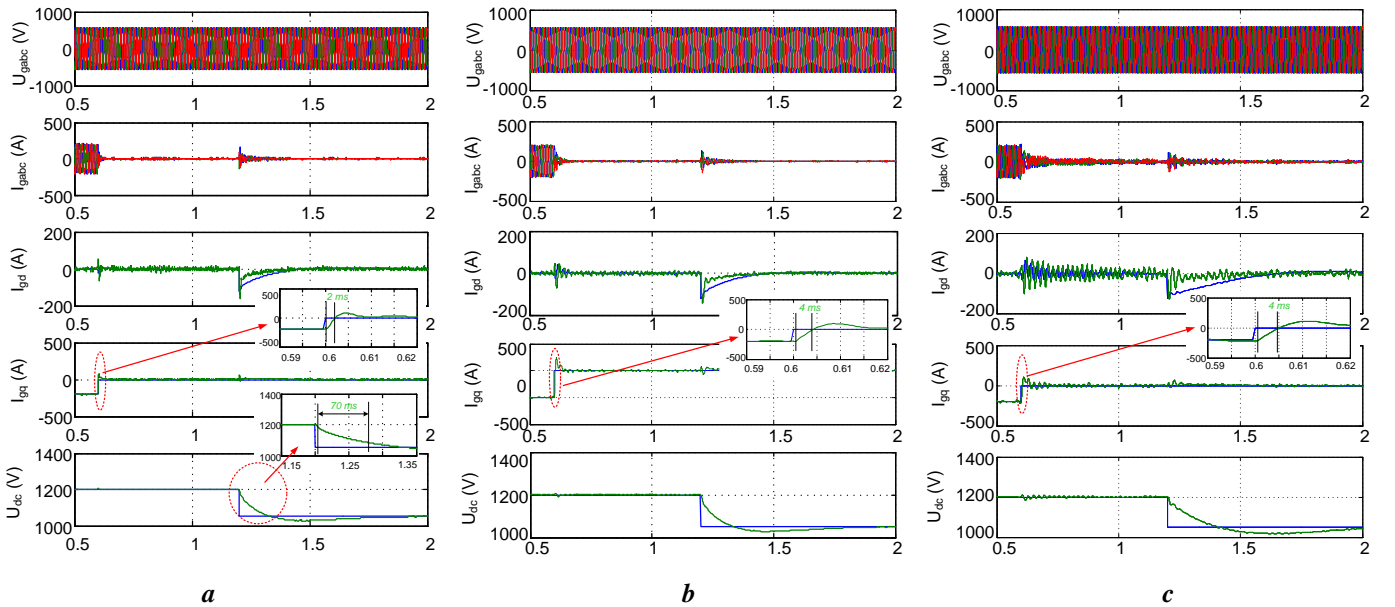
Fig. 7 *Simulation results of the grid-side converter in the 2 MW system*

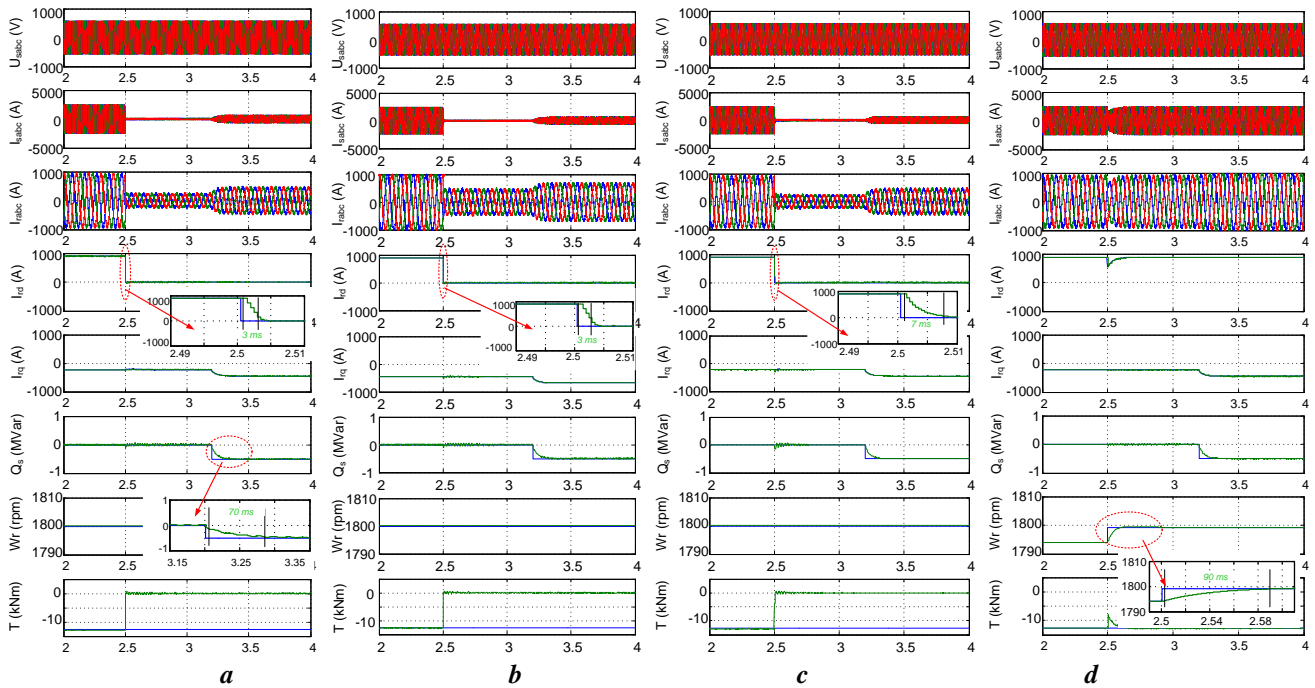*a Step response of inner grid current loop and outer dc voltage loop*
b Step response of inner grid current with two times of the grid filter
c Step response of inner grid current with bandwidth of 70 Hz

As the d-axis and the q-axis current loops of the GSC have the same transfer function, the bandwidth of the current loop can simply be verified by using a step response at the q-axis reference. As shown in Fig. 7a, a 200 A over-excited reactive current is set to unity power factor at the instant of 0.6 second, and its

corresponding rise time can be seen around 2.0 ms, which agrees with the theoretical rise time. Similarly, a step change of the dc-link voltage from 1200 V to 1050 V is applied at the instant of 1.2 second, a rise time around 70 ms can be observed, which proves the designed bandwidth as calculated. Moreover, in order to illustrate the robustness of the designed PI controller, Fig. 7b shows the case that the grid filter becomes two times of the original value. It can be seen that it takes about 4 ms to track to abrupt changing current reference, as the bandwidth of the grid current decreases from 100 Hz to 60 Hz due to the higher inertia of the grid filter. Furthermore, if the bandwidth of the grid current loop is designed at 70 Hz, the rising time during the reactive current step changes to 4 ms as shown in Fig. 7c, which indicates that the proposed PI controller has a better dynamic performance.
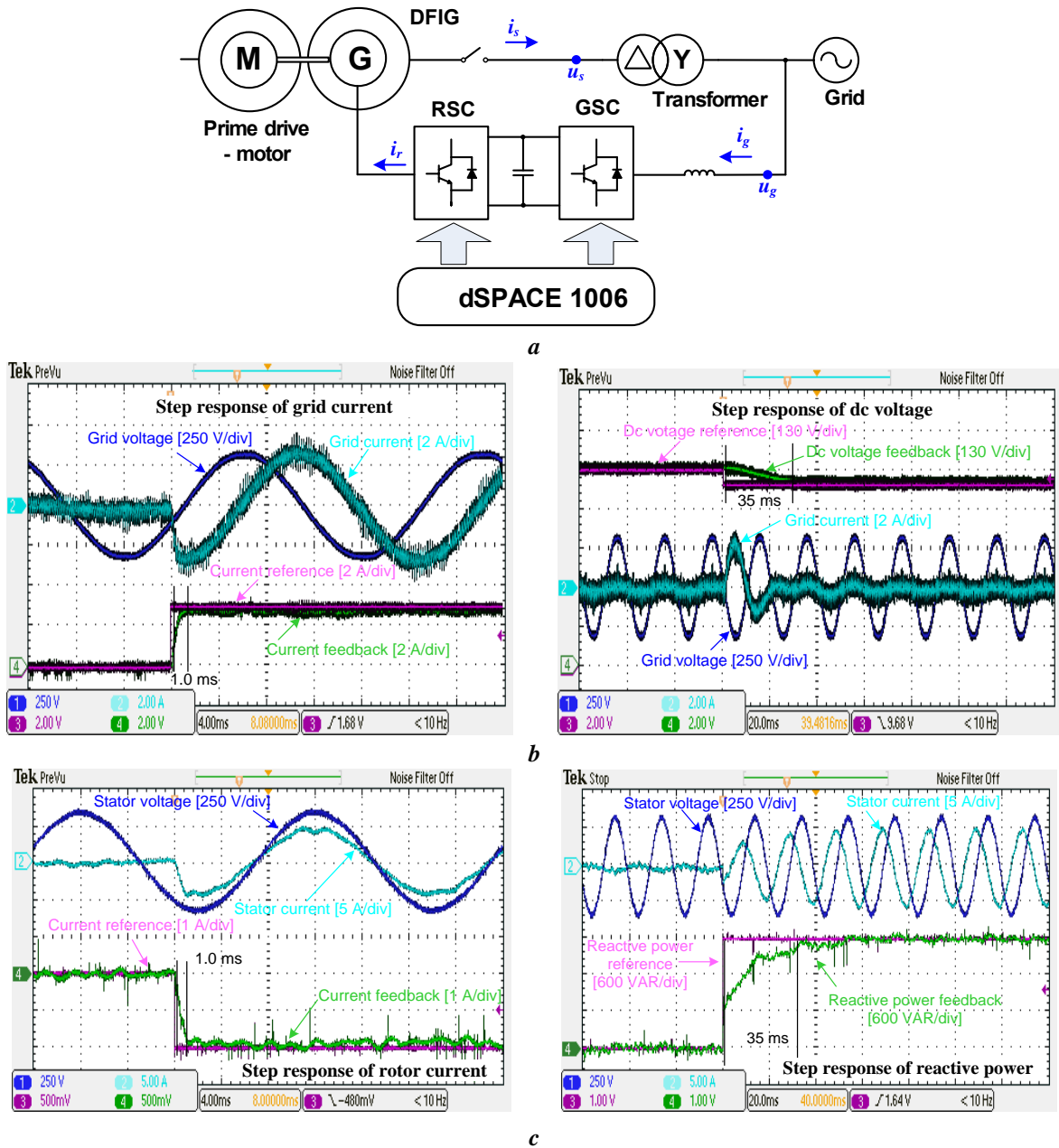

Fig. 8 *Simulation results of the rotor-side converter inner loop and outer loop in the 2 MW system*

a Step response of inner rotor current loop and outer reactive power loop
b Step response of inner rotor current with half of the magnetizing inductance
c Step response of inner rotor current with bandwidth of 50 Hz
d Step response of and outer speed loop

Due to the outer loops of the rotor speed and the reactive power in the RSC, it is impossible to verify the step response time for the inner rotor current. As a result, the inertia of the DFIG is assumed infinite to neglect the rotor speed loop and keep a constant rotor speed. Under this circumstance, a step of the d-axis rotor current in terms of 500 A and a reactive power in terms of 0.5 MVar can be applied at the instants of 2.5 and 3.2 second. As shown in Fig. 8a, their rise time can be found at 3.0 ms and 70 ms, both of which are consistent with the expected rise time. Besides, as shown in Fig. 8b, when the magnetizing inductance reduces to a half of the original value, the step response time is still around 3 ms because the plant of the

16

rotor current is irrelevant with the magnetizing inductance. Furthermore, in the case that the current bandwidth is designed at 50 Hz with varied PI parameters, the rising time is prolonged to 7 ms as shown in Fig. 8c. If the torque equation of the DFIG is taken into account as shown in Fig. 8d, the rising time of the rotor speed is around 90 ms during a step of the rotor speed, which is consistent with the designed 3 Hz bandwidth.

a

b

c

Fig. 9 *Experimental verification in a 7.5 kW DFIG system*

a Setup of the test rig
b Experimental results of the grid-side converter to verify the dual-loop bandwidth
c Experimental results of the rotor-side converter to verify the dual-loop bandwidth

In order to experimentally validate the designed bandwidth of the control loop, a down-scaled 7.5 kW test system is shown in Fig. 9a. The DFIG is externally driven by a prime motor, and the back-to-back power converters are linked to the grid through a boost inductor. Two 5.5 kW Danfoss motor drives are used for the GSC and the RSC, both of which are controlled by dSPACE 1006, using a sampling frequency of 10 kHz and a switching frequency of 5 kHz.

In respect to the bandwidth verification of the GSC, with the same PI parameters of the current controller, the rise time during a 3 A step change of the reactive current can be found around 1.0 ms as shown in Fig. 9b, which is almost the same compared to the theoretically designed bandwidth of 300 Hz. Afterwards, a dc-voltage step change is used to test the bandwidth of the voltage loop. If the dc-link voltage is changed from 650 V to 600 V, a rise time of 35 ms can be found, which validates the bandwidth of 10 Hz.

In respect to the RSC, the bandwidth of the dual loop is shown in Fig. 9c. With the same controller parameters as illustrated in the theoretical design, the active current reference is changed to 2 A, a step response around 1 ms can be found, which is consistent with the designed 350 Hz bandwidth. Then, a reactive power step of 1.8 kVar is performed, and a rise time of 35 ms can be found, which is the same as the designed bandwidth of 10 Hz.

4. Conclusion

By using the traditional vector control, this paper focuses on the PI controller design of the back-to-back power converters equipped with the doubly-fed induction generator system. The model of the power converter can be achieved by using the synchronous reference frame together with the linear PWM model. Accordingly, the dual loop design can be implemented in terms of the inner current loop and outer voltage/power loop. Regardless of the back-to-back power converters, it is concluded that the bandwidth design of the inner current should be maintained between 1/20 and 1/10 of the switching frequency for the fast response and the switching harmonic mitigation. Moreover, the bandwidth of the outer voltage/power is preferred to be regulated from 1/50 to 1/10 of the inner loop in order to fully decouple the dual loop. The procedure of the dual-loop bandwidth design for the grid-side converter and the rotor-side converter are thoroughly addressed and explained on a real-scale 2 MW and a down-scaled 7.5 kW DFIG systems. On the basis of the relationship between the bandwidth and the rise time, the theoretical designed bandwidth is able to be verified by using the step response in both the simulations and the experiments.

5. References

[1] V. Yaramasu, B. Wu, P. C. Sen, S. Kouro, and M. Narimani, "High-power wind energy conversion systems: state-of-the-art and emerging technologies," *in Proceedings of the IEEE*, vol. 103, no. 5, pp. 740-788, May 2015.

[2] North American wind power. *Top 15 Wind turbine suppliers of 2013 revealed.* (http://www.nawindpower.com)

[3] F. Blaabjerg, and K. Ma, "Future on power electronics for wind turbine systems," *IEEE Journal of Emerging and Selected Topics in Power Electronics*, vol. 1, no. 3, pp. 139-152, Sep. 2013.

[4] M. Liserre, R. Cardenas, M. Molinas, and J. Rodriguez, "Overview of multi-MW wind turbines and wind parks," *IEEE Trans. on Industrial Electronics*, vol. 58, no. 4, pp. 1081-1095, Apr. 2011.

[5] R. Cardenas, R. Pena, S. Alepuz, and G. Asher, "Overview of control systems for the operation of DFIGs in wind energy applications," *IEEE Trans. on Industrial Electronics*, vol. 60, no. 7, pp. 2776-2798, Jul. 2013.

[6] G. Abad, J. Lopez, M. Rodriguez, L. Marroy, and G. Iwanski. *Doubly Fed Induction Machine: Modeling and Control for Wind Energy Generation Applications*. Wiley-IEEE Press, 2011.

[7] E. Tremblay, S. Atayde, and A. Chandra, "Comparative study of control strategies for the doubly fed induction generator in wind energy conversion systems a DSP-based implementation approach," *IEEE Trans. on Sustainable Energy*, vol. 2, no. 3, pp. 288-299, 2011.

[8] L. Xu, "Coordinated control of DFIG's rotor and grid side converters during network unbalance," *IEEE Trans. on Power Electronics*, vol. 23, no. 3, pp. 1041-1049, May 2008.

[9] J. Hu, Y. He, L. Xu, and B. W. Williams, "Improved control of DFIG systems during network unbalance using PI–R current regulators," *IEEE Trans. on Industrial Electronics*, vol. 56, no. 2, pp. 439-451, Feb. 2009.

[10] J. Arbi, M. J. B. Ghorbal, I. Slama-Belkhodja, and L. Charaabi, "Direct virtual torque control for doubly fed induction generator grid connection," *IEEE Trans. on Industrial Electronics*, vol. 56, no. 10, pp. 4163-4173, Oct. 2009.

[11] D. Santos-Martin, J. L. Rodriguez-Amenedo, and S. Arnalte, "Direct power control applied to doubly fed induction generator under unbalanced grid voltage conditions," *IEEE Trans. on Power Electronics*, vol. 23, no. 5, pp. 2328-2336, Sep. 2008.

[12] D. N. Zmood, and D. G. Holmes, "Stationary frame current regulation of PWM inverters with zero steady-state error," *IEEE Trans. on Power Electronics*, vol. 18, no. 3, pp. 814-822, May 2003.

[13] F. Blaabjerg, R. Teodorescu, M. Liserre, and A. V. Timbus, "Overview of control and grid synchronization for distributed power generation systems," *IEEE Trans. on Industrial Electronics*, vol. 53, no. 5, pp. 1398-1409, Oct. 2006.

[14] M. Liserre, R. Teodorescu, and F. Blaabjerg, "Multiple harmonics control for three-phase grid converter systems with the use of PI-RES current controller in a rotating frame," *IEEE Trans. on Power Electronics*, vol. 21, no. 3, pp. 836-841, May 2006.

[15] V. Blasko, and V. Kaura, "A new mathematical model and control of a three-phase AC-DC voltage source converter," *IEEE Trans. on Power Electronics*, vol. 12, no. 1, pp. 116-123, Jan 1997.

[16] R. Pena-Alzola, M. Liserre, F. Blaabjerg, R. Sebastian, J. Dannehl, and F. W. Fuchs, "Systematic design of the lead-lag network method for active damping in LCL-filter based three phase converters," *IEEE Trans on Industrial Informatics*, vol. 10, no. 1, pp. 43-52, Feb. 2014.

[17] M. Liserre, F. Blaabjerg, and S. Hansen, "Design and control of an LCL-filter-based three-phase active rectifier," *IEEE Trans. on Industry Applications*, vol. 41, no. 5, pp. 1281-1291, Sep. 2005.

[18] R. Teodorescu, M. Liserre, and P. Rodriguez. *Grid converters for photovoltaic and wind power systems*. John Wiley & Sons, 2011.

[19] D. G. Holmes, T. A. Lipo, B. P. McGrath, and W. Y. Kong, "Optimized design of stationary frame three phase AC current regulators," *IEEE Trans. on Power Electronics*, vol. 24, no. 11, pp. 2417-2426, Nov. 2009.

[20] M. P. Kazmierkowski, R. Krishnan, and F. Blaabjerg. *Control in power electronics: selected problems*. Academic press, 2002.

[21] B. Wen, D. Boroyevich, R. Burgos, P. Mattavelli, and Z. Shen, "Small-signal stability analysis of three-phase ac systems in the presence of constant power loads based on measured d-q frame impedances," *IEEE Trans. on Power Electronics*, vol. 30, no. 10, pp. 5952-5963, Oct. 2015.

[22] H. Mao, D. Boroyevich, and F. C. Y. Lee, "Novel reduced-order small-signal model of a three-phase PWM rectifier and its application in control design and system analysis," *IEEE Trans. on Power Electronics*, vol. 13, no. 3, pp. 511-521, May 1998.

[23] A. Bryson. *Applied optimal control: optimization, estimation and control*. CRC Press, 1975.